BIOCHEMISTRY
including biophysical chemistry & molecular biology
Article

Biochemistry **2009,** *48,* 9831–9838 9831
DOI: 10.1021/bi900545e

Lipidic Sponge Phase Crystal Structure of a Photosynthetic Reaction Center Reveals Lipids on the Protein Surface†

Annemarie B. Wöhri,‡ Weixiao Y. Wahlgren,§ Erik Malmerberg,§ Linda C. Johansson,§ Richard Neutze,§ and Gergely Katona*,§

‡*Department of Chemical and Biological Engineering, Molecular Biotechnology, Chalmers University of Technology, SE-405 30 Gothenburg, Sweden, and* §*Department of Chemistry, Biochemistry, and Biophysics, University of Gothenburg, SE-405 30 Gothenburg, Sweden*

Received March 31, 2009; Revised Manuscript Received September 9, 2009

ABSTRACT: Membrane proteins are embedded in a lipid bilayer and maintain strong interactions with lipid molecules. Tightly bound lipids are responsible for vertical positioning and integration of proteins in the membrane and for assembly of multisubunit complexes and occasionally act as substrates. In this work we present the lipidic sponge phase crystal structure of the reaction center from *Blastochloris viridis* to 1.86 Å, which reveals lipid molecules interacting with the protein surface. A diacylglycerol molecule is bound, through a thioether bond, to the N-terminus of the tetraheme cytochrome *c* subunit. From the electron density recovered at the Q_B site and the observed change in recombination kinetics in lipidic sponge phase-grown crystals, the mobile ubiquinone appears to be displaced by a monoolein molecule. A 36 Å long electron density feature is observed at the interface of transmembrane helices belonging to the H- and M-subunits, probably arising from an unidentified lipid.

Photosynthesis, the conversion of light into chemical energy by living organisms, arose approximately 3.5 billion years ago, early in the history of life on Earth. It is one of the most important biological processes in nature and plays an essential role in the energetic and metabolic macrocycle of the biosphere. It originates from the kingdom of Bacteria, from a period when the level of molecular oxygen was low in the atmosphere (*1*). *Blastochloris viridis* (formerly known as *Rhodopseudomonas viridis*) is a non-sulfur purple bacterium, which contains important characteristics present in oxygenic photosynthetic systems but predates them (*2*, *3*). The *B. viridis* reaction center (RC_{vir})[1] is structurally homologous to D1/D2 subunits of photosystem II (PSII), and therefore it is often considered as a model system for oxygenic photosynthesis. It was also the first integral membrane protein from which a high-resolution structure was obtained (*4*). This X-ray structure was achieved using detergent-based crystallization methods, and continuous improvements have extended the resolution of detergent-based crystals to 1.96 Å (*5*).

Membrane proteins consist of a hydrophilic and a hydrophobic part and must be extracted from their native membrane using detergents prior to crystallization. While lipidic cubic phase crystallization (LCP) still requires purified detergent-solubilized protein as a starting point, it was developed specifically to tackle the difficulties related to the long-term loss of native environment during membrane protein crystallization (*6*). In this method detergents are substituted by lipids such as monoolein as the crystallization medium. The LCP method has been used for the successful crystallization of the photosynthetic reaction center from *Rhodobacter sphaeroides* (RC_{sph}) (*7*−*9*) and has been developed further into a lipidic sponge phase- (LSP-) based crystallization sparse matrix screen (*10*). LSP-grown crystals have generated a number of membrane protein X-ray structures including the photosynthetic reaction center from *R. sphaeroides* (*11*, *12*), the cobalamin transporter BtuB (*13*), and a bacterial light harvesting complex II (*14*).

Here we present the crystal structure of the photosynthetic reaction center from *B. viridis*, which was crystallized using the LSP technique and diffracted to 1.86 Å. By taking advantage of the type I crystal form, the orientation and position of the reaction center could be established in the lipid bilayer. A diacylglycerol lipid appeared covalently bound to the tetraheme cytochrome *c* subunit, which has not previously been seen when crystallizing with detergent-based methods. Monoolein, the major constituent of the LSP matrix, was observed at three locations including the Q_B pocket. In addition, a 36 Å long elongated electron density feature was observed at the interface of the H- and M-subunit, which probably corresponds to an unidentified lipid.

MATERIALS AND METHODS

The bacterial strain ATCC 19567 from *B. viridis* was ordered from Deutsche Sammlung von Mikroorganismen and Zellkulturen GmbH (DSMZ). Monoolein (1-monooleyl-*rac*-glycerol) was purchased from Sigma (99% purity), and 1,2,3-heptanetriol (high melting point isomer) and the detergent *N*,*N*-dimethyldodecylamine *N*-oxide (LDAO) were bought from Fluka Chemika. Jeffamine M-600 and the crystallization additive 1 M trisodium citrate were obtained from Hampton Research. The POROS HQ anion-exchange chromatography column was ordered from

†This work was supported by the Swedish Science Research Council (VR), HFSP, the European Commission (FLASH, EMEP), the Harald and Greta Jeanssons Foundation, and EMBO.

*To whom correspondence should be addressed. Tel: +46 31 786 3959. Fax: +46 31 786 3910. E-mail: gergely.katona@chem.gu.se.

[1]Abbreviations: RC_{vir}, photosynthetic reaction center from *Blastochloris viridis*; RC_{sph}, photosynthetic reaction center from *Rhodobacter sphaeroides*; LCP, lipidic cubic phase; LSP, lipidic sponge phase; PSII, photosystem II.

Published on Web 09/10/2009

Applied Biosystems and the HiPrep 16/60 Sephacryl S-200 high-resolution gel filtration chromatography column from GE Healthcare. The LSP kit was obtained from Molecular Dimensions Ltd. (*10*).

Purification and Crystallization of RC_{vir}. The purification protocol of RC_{vir} was adopted from ref *15* with the following modifications. For solubilization LDAO was added dropwise up to 4% to the membrane mixture and stirred for 3 h at room temperature in darkness. The solubilized membranes were ultracentrifuged for 90 min, 4 °C, 175000*g*, and the obtained protein solution was adjusted to pH 8.5 and applied to a high binding capacity anion-exchange chromatography column (POROS HQ), which was equilibrated with 20 mM Tris-HCl, pH 8.5, and 1% LDAO prior to usage. The protein was eluted with a continuous salt gradient (0−500 mM NaCl in 20 mM Tris-HCl, pH 8.5, and 1% LDAO). Further impurities were removed by a high-resolution HiPrep 16/60 Sephacryl S-200 gel filtration chromatography step (buffer: 10 mM Tris-HCl, pH 8.5, 0.1% LDAO, and 0.1 mM EDTA). Finally, the buffer was exchanged by three cycles of concentration and dilution (approximately 10× the concentrated volume) with a 20 mM sodium phosphate, pH 6.8, 0.1% LDAO, and 10 μM EDTA buffer in a 100 kDa MWCO Vivaspin (Sartorius AG) concentrator before a final concentration step to 20−25 mg/mL. The optical purity ratio (A_{280}/A_{830}) of this sample was approximately 2.1.

Crystals were grown using the LSP crystallization technique as described previously (*11*). Initial crystal hits were obtained with condition 37 of the LSP kit (*10*). As reservoir solution 0.55 M sodium acetate, 0.75 M HEPES, pH 6.3, 0.1 g/mL Na/K-PO_4 has been used, and 1 μL of protein solution was mixed with 1 μL of LSP in a hanging-drop, vapor-diffusion experiment. Final conditions were obtained by mixing monoolein with water in a ratio of 60:40 (v/v) until a viscous, nonbirefringent LCP was formed. Thereafter, LSP initiating solution (20% Jeffamine M-600, 1 M HEPES, pH 8.0, 0.7 M $(NH_4)_2SO_4$, and 2.5% 1,2,3-heptanetriol) was added in a ratio of 1 to 4 (v/v) and equilibrated until phase separation has occurred. The upper LSP was harvested, and 1 μL was used as a precipitant solution together with 1 μL of protein solution and 1 μL of additive 1 M trisodium citrate in a hanging-drop, vapor-diffusion experiment. The crystallization plates were stored in darkness at room temperature, and diamond-shaped crystals appeared after 2 weeks, growing to a maximum size of 0.25 mm × 0.25 mm × 0.15 mm. The crystals were harvested directly from the LSP without addition of lipase or cryoprotectants.

X-ray Diffraction Studies. Lower dose X-ray data were collected at 100 K with an ADSC Q4R CCD detector at ID14-eh3 of the ESRF (λ = 0.931 Å). The oscillation range per image was 0.5°. Higher dose X-ray data were collected at the SLS (λ = 0.992 Å) at 100 K using a PILATUS 6M detector with continuous data collection mode. The detector was read out after every 0.1° rotation of the crystal. Low-dose data was indexed and integrated with MOSFLM, scaled with SCALA, while high-dose data was processed with XDS and XSCALE (*16*) for optimal treatment of the very finely sliced reflections. Subsequent data processing was carried out in the CCP4 program suite (*17*). The crystals belong to space group $P2_12_12$, and data statistics are summarized in Table 1. The structures were solved independently by molecular replacement using the program AMoRe (*18*). The starting coordinates were taken from the detergent-based crystal structure (PDB entry 2PRC) (*19*) and included the protein moiety only. The rotational search in the resolution range 15−3 Å resulted in a single peak far above the noise level. The translational search assuming the space group $P2_12_12$ produced the highest peak. At this point a random selection of approximately 5% of the data (test set) was assigned for calculation of the free *R*-factor and was not included in the refinement. The phases from the molecular replacement solution were used in automated rebuilding of the protein subunits using the program Arp/wArp (*20*). Even though the automated procedure did not model cofactors, Arp/wArp was able to find and dock more than 90% of the residues of the final model in both structures. The models were systematically improved through iterative cycles of manual rebuilding by means of Coot (*21*) and crystallographic refinement using the program REFMAC5 (*22*). The models were checked by cross-validated SigmaA weighted electron density maps calculated with both $2mF_o - DF_c$ and $mF_o - DF_c$ coefficients (*23*). At the final steps of refinement of both structures a TLS (*24*) model of the four polypeptide chains were used, which resulted in the improvement of the R_{free} value by approximately 2%. The quality and stereochemistry of the models were monitored during the refinement with PROCHECK (*25*) and Molprobity (*26*). The absorbed X-ray dose during data collection was estimated by the program RADDOSE (*27*). The occupancy of the monoolein in the Q_B binding pocket was estimated using the assumption that the average *B*-factors of the glycerol moiety of the lipid are similar to the interacting amino acid residues and the nearest water

Table 1: Crystallographic Data and Refinement Statistics

	low-dose data set	high-dose data set
PDB entry	2WJM	2WJN
resolution (Å)[a]	45.9−1.95 (2.06−1.95)	45.0−1.86 (2.00−1.86)
space group	$P2_12_12$	$P2_12_12$
unit cell dimensions, *a*, *b*, *c* (Å)	84.5, 138.5, 177.8	84.8, 139.4, 178.2
total absorbed dose (Gy)	4.4×10^6	7.1×10^7
no. of unique reflections[a]	145856 (18911)	176119 (34206)
completeness (%)[a]	96.2 (86.4)	97.8 (92.1)
multiplicity[a]	4.3 (3.6)	6.6 (6.7)
$\langle I/\sigma \rangle$[a]	10.9 (2.1)	15.0 (3.7)
R_{sym} (%)[a,b]	8.9 (72.6)	6.8 (48.5)
R/R_{free} (%)[c]	17.3/20.1	16.6/19.3
rmsd from ideal bond lengths (Å)/angles (deg)	0.017/2.1	0.018/2.3
no. of atoms (protein/waters/hetero)	9186/711/774	9175/692/723
Ramachandran plot (% by PROCHECK)		
most favored	92.0	92.4
additionally allowed	7.5	7.1
generously allowed	0.4	0.4
disallowed	0.1	0.1
average *B*-factors (Å^2)	33.0 ± 6.1	37.0 ± 6.8
protein[d]	32.6 ± 4.5	36.6 ± 5.2
waters	37.3 ± 8.8	44.4 ± 10.5
all other heteroatoms	34.2 ± 13.8	35.5 ± 13.3
diacylglycerol	66.1 ± 8.1	
monoolein 1 (at Q_B site 70% occupancy)	42.8 ± 4.1	47.0 ± 6.1
monoolein 2	55.7 ± 1.6	64.2 ± 1.2
monoolein 3	59.6 ± 12.5	64.0 ± 4.4

[a]Values in parentheses indicate statistics for the highest resolution shell. [b]$R_{sym} = \sum|I_o - \langle I \rangle|/\sum I_o \times 100$, where I_o is the observed intensity of a reflection and $\langle I \rangle$ is the average intensity obtained from multiple observations of symmetry-related reflections. [c]*R* factor $= \sum||F_o| - |F_c||/\sum|F_o| \times 100$. [d]Residual *B*-factors after TLS refinement.

molecule. Superposition of the detergent and LSP-based crystal structures was performed with the program LSQMAN (*28*) using all equivalent C_α atoms. $2F_o - F_c$ electron density maps of PDB entries 1VRN (*29*) and 2J8C (*30*) were obtained from the Uppsala Electron Density Server (*31*). Figures were generated with PYMOL (*32*).

Charge Recombination Kinetics. Time-resolved absorption measurements were performed on RC_{sph} both in detergent solution (0.1 mM RC_{sph} in 0.1 M HEPES, pH 7.5, and 0.1% (w/v) LDAO) and in LSP-grown crystals (20% Jeffamine M-600, 1 M HEPES, pH 8.1, 0.7 M $(NH_4)_2SO_4$ and 2.5% 1,2, 3-heptanetriol) (*11*). The crystal samples were mounted in a 0.8 mm quartz capillary (Hampton Research), sealed using wax, and a small aliquot of mother liquid was added to the capillary to prevent dehydration. The absorption changes at 865 nm were recorded using a single-beam microspectrophotometer (*33*) (XSPECTRA, 4DX systems AB) with a SD2000 monochromator/detector system (Ocean Optics Inc.). Flash excitation of the sample was provided by a frequency-doubled Nd:YAG laser (Spectra-Physics; 532 nm, 6 ns) synchronized to the microspectrophotometer using a setup of local design (*34*). Time-resolved data were collected in the range of 1 ms to 6 s with each data point averaged over five acquisitions (1 Hz repetition rate, 0.7 mJ/pulse).

Protein Data Bank Accession Number. The refined crystallographic structure and crystallographic observations have been deposited in the Protein Data Bank under entries 2WJM and 2WJN.

RESULTS AND DISCUSSION

LSP-Grown Crystals of Reaction Center from B. viridis. Crystals of RC_{vir} were grown using the LSP crystallization method in the presence of monoolein and diffracted up to 1.86 Å resolution. These crystals, unlike all previous Protein Data Bank (*35*) entries of RC_{vir} (*36*), belong to space group $P2_12_12$ and show one molecule per asymmetric unit. Two data sets were collected, which differed by more than 10-fold in absorbed radiation dose, from different crystals prepared in an identical way. X-ray diffraction data and final refinement statistics of the two data sets are summarized in Table 1. The high-dose data set presented in this work shows improved resolution of the structure, but it also illustrates the effect of specific radiation damage. Therefore, the main structural conclusions are derived from the low-dose data set, and the high-dose data set is used only for discussion on radiation damage. The structure was solved by molecular replacement using an X-ray structure from detergent-grown crystals (PDB entry 2PRC) (*19*) as a starting model. The RC_{vir} molecules are arranged within stacked antiparallel planes in the crystal (Figure 1A) similar to RC_{sph} grown from LCP and LSP (*8*, *11*) (Figure 1B). Crystal contacts within the membrane plane are not observed, unlike in crystals of RC_{sph} where a bound cardiolipin headgroup establishes a strong lateral crystal contact (*8*).

Figure 2 shows the reaction center with the estimated boundaries between the hydrophobic and hydrophilic regions of the crystal. The boundaries are defined by two planes parallel with the *ab* crystallographic plane in the asymmetric unit at *Z*-coordinates (coordinates $Z = 16$ and 50 Å, respectively) which define a hydrophobic slab with a thickness of 34 Å accounting for approximately 39% of the crystal volume. The approximate positions of the delimiting planes along the *c*-axis were estimated by the outermost layer of solvent-exposed Trp, Phe, and Tyr

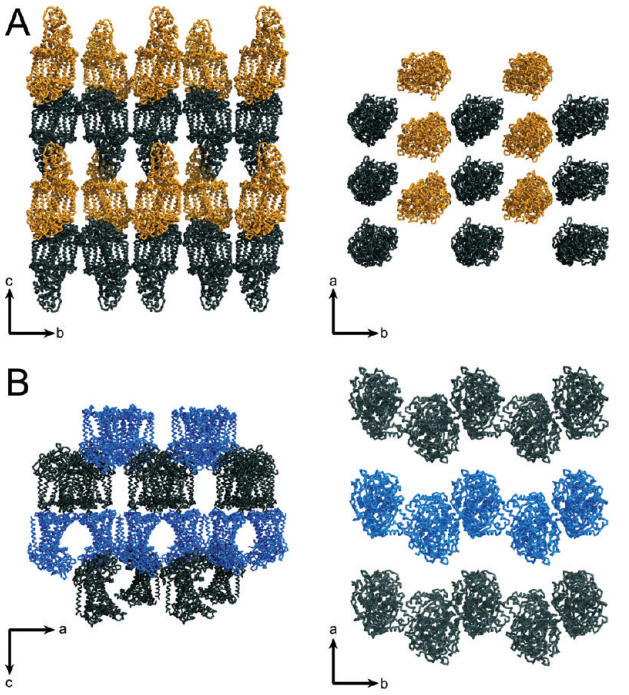

FIGURE 1: (A) Type I crystal packing of RC_{vir} grown from the LSP. The protein molecules are stacked in antiparallel planes. Left: The viewing direction is parallel with the *ab* (membrane) plane. Right: The viewing direction is parallel to the *c*-axis. (B) For comparison the type I crystal packing of RC_{sph} obtained from the LCP is shown (PDB entry 1OGV) (*8*). Left: The viewing direction is parallel with the *ab* (membrane) plane. Right: The viewing direction is parallel to the *c*-axis.

residues represented as stick models in Figure 2 (cytoplasmic side, Tyr-M3, Tyr-M7, Trp-M23, Phe-M33, Trp-M37, Phe-H96; periplasmic side, Phe-C2, Trp-L59, Trp-L142, Phe-L254, Phe-L271, Phe-M79, Trp-M112, Phe-M288). Moreover, these delimiting planes do not conflict with hydrophilic subunits of symmetry-related molecules in the adjacent bilayers.

In the LCP- and LSP-grown RC_{sph} crystals the position of symmetry-related cofactors of the L- and M-branch are approximately the same along the membrane normal (*8*, *11*). In contrast, in the LSP-grown RC_{vir} crystals the active L-branch is shifted toward the direction of the cytoplasm relative to the inactive M-branch. This arises because the 2-fold pseudosymmetry axis of RC_{vir} tilts in another direction, relative to the normal of the membrane, to that seen in the LSP crystal structure of RC_{sph}. The magnitude of the shift is given by $i_v = \vec{i} \cdot \vec{n}$, where $\vec{i}$ is the vector connecting the pseudosymmetry-related magnesium ions of the accessory chlorophylls and $\vec{n}$ is the normal vector of the membrane and equates to 2.6 Å displacement along the normal vector. Supporting Information Figure 1 describes in detail how the tilts of the reaction centers in the membrane were calculated.

Residues 46−60 of the H-subunit of RC_{vir} are disordered in the LSP crystal structure (Figure 3A) and are not visible in the electron density. In contrast, in the detergent-based crystals this region is stabilized by crystal contacts of the transmembrane helices of two symmetry-related reaction centers: the H-subunit in molecule 1 and the L-subunit of molecule 2. Residues Arg-H80 to Thr-H85 thus deviate after superposition by more than 6.5 Å compared to the detergent-based structure, which is also influenced by crystal contacts (Figure 3B,C). However, in this case, packing interactions in the LSP-grown crystal form alter the native conformation of the loop.

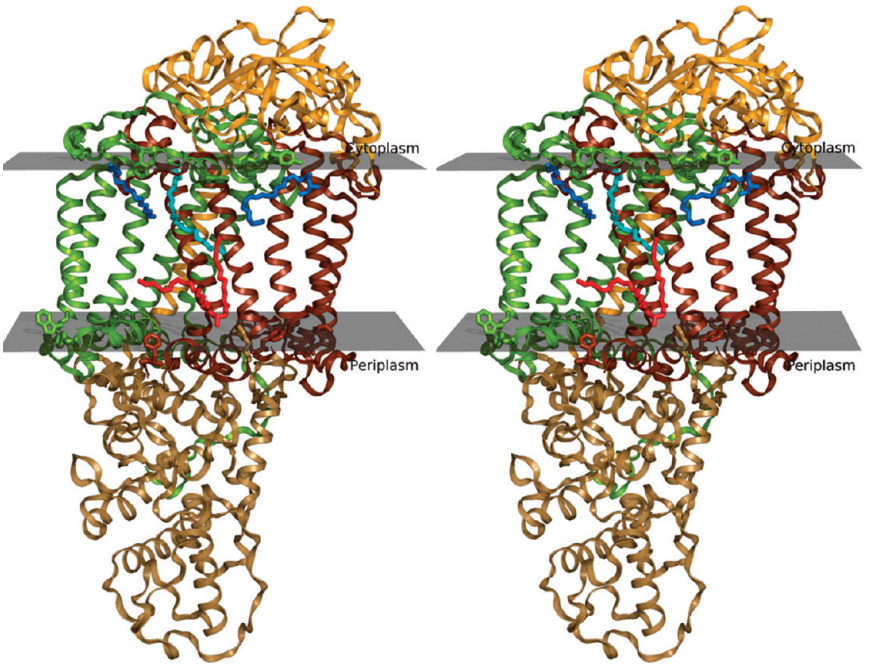

FIGURE 2: Stereoview of the overall arrangement of lipids bound to the surface of RC_{vir} in the low-dose data set: one diacylglycerol (red) and two monoolein molecules outside (blue) and one monoolein inside (cyan) the Q_B binding pocket. The colors of the ribbons representing the protein subunits are as follows: tetraheme cyctochrome *c* (beige), L-subunit (brown), M-subunit (green), and H-subunit (orange). The approximate position of the membrane is indicated with transparent planes.

Covalently Bound Diacylglycerol on the N-Terminus of the Cytochrome c Subunit. LSP-grown crystals revealed lipids bound to the surface of the protein. Figure 2 shows the overall fold of the RC_{vir} and four modeled lipids on the protein surface: a covalently bound diacylglycerol lipid (red) and three monoolein molecules (two blue and one cyan). The cyan-colored monoolein occupies the Q_B ubiquinone binding pocket (see below). On the periplasmic side a covalently bound lipid was observed at the N-terminal cysteine of the tetraheme cytochrome *c* subunit (Figure 4A,B). Previous mass spectrometry studies (*37*) identified this lipid as a diacylglycerol molecule covalently attached to the cysteine side chain through a thioether bond. One of the fatty acid tails is situated in a well-defined groove and interacts with the accessory bacteriochlorophyll of the M-branch by van der Waals forces. The other fatty acid moiety is weaker in electron density and points perpendicular to the plane of the membrane. This prokaryotic posttranslational modification facilitates the association of the tetraheme cytochrome *c* subunit to the membrane and presumably assists the organization of quaternary structure. Similar, but reversible modification (thioacylation) can be observed in eukaryotes on cysteines of G protein-coupled receptors and G proteins (*38*) where the modification plays a regulatory role and also leads to the nonrandom distribution of specific membrane lipids and proteins. It is puzzling why in the detergent-based crystal form there is no indication of this covalent posttranslation modification, which was detected by mass spectrometry in the detergent-solubilized protein. For example, in the 1.96 Å resolution crystal structure by Li et al. (*5*) (PDB entry 2I5N) there is no indication of an attached thioether bond. One possibility is that the crystal contacts interfere with the diacylglycerol in the detergent-based crystal form; however, there is not any crystal contact in close vicinity, which could interfere with the lipid. Radiation damage, if the X-ray absorption is not controlled, might also provide an explanation for the disappearance of the thioether bond.

Radiation Sensitivity of the Thioether Bond. While chemically relatively stable, the thioether bond, which connects the diacylglycerol to the N-terminal cysteine of the cytochrome c subunit, is sensitive to radiation damage. A high-dose data set (Table 1) was collected to illustrate the effect of specific radiation damage in the structure. Electron density recovered from this high-dose data set shows reduced occupancy of the sulfur atom and the lipid moiety. In Figure 4C a negative $F_o - F_c$ electron density (red) appears on the sulfur atom of the N-terminal cysteine, and the $2F_o - F_c$ electron density of the thioether bond is no longer continuous when contoured at the same σ level as in Figure 4B.

Radiation damage is a complex phenomenon, and according to the widely accepted model it has a general and specific form (*39*). Specific radiation damage affects the electron density of specific parts of the structure, and different chemical bonds may have very different dose dependence. Bonds involving heavier atoms are more affected. For example, disulfide bridges containing sulfurs are more easily broken than carbon−carbon bonds. In contrast, general radiation damage manifests as a dose-dependent decay of I/σ of the reflections, which is (more or less) similar in different protein crystals and typically reaches a factor of 0.5 at an absorbed dose of approximately 2×10^7 Gy (so-called Henderson limit (*40*)).

Comparison of the high- and low-dose structures shows a high degree of general similarity with a 0.16 Å rmsd after superposing all (1171) C_α atoms. When looking at site-specific differences, we find only residues Cys-C1, Glu-C85, Gln-L55, Tyr-H41, Phe-H96, and Glu-H119 in which at least one of the side chain atoms deviates by more than 1 Å. In addition, Glu-L82 is present in two conformations in the low-dose data set, one of which deviates significantly from the high-dose conformation. Nonisomorphism between the crystals could provide an alternative explanation why these residues differ in conformation. If the molecules are slightly shifted from one another in the crystal lattice, the residues

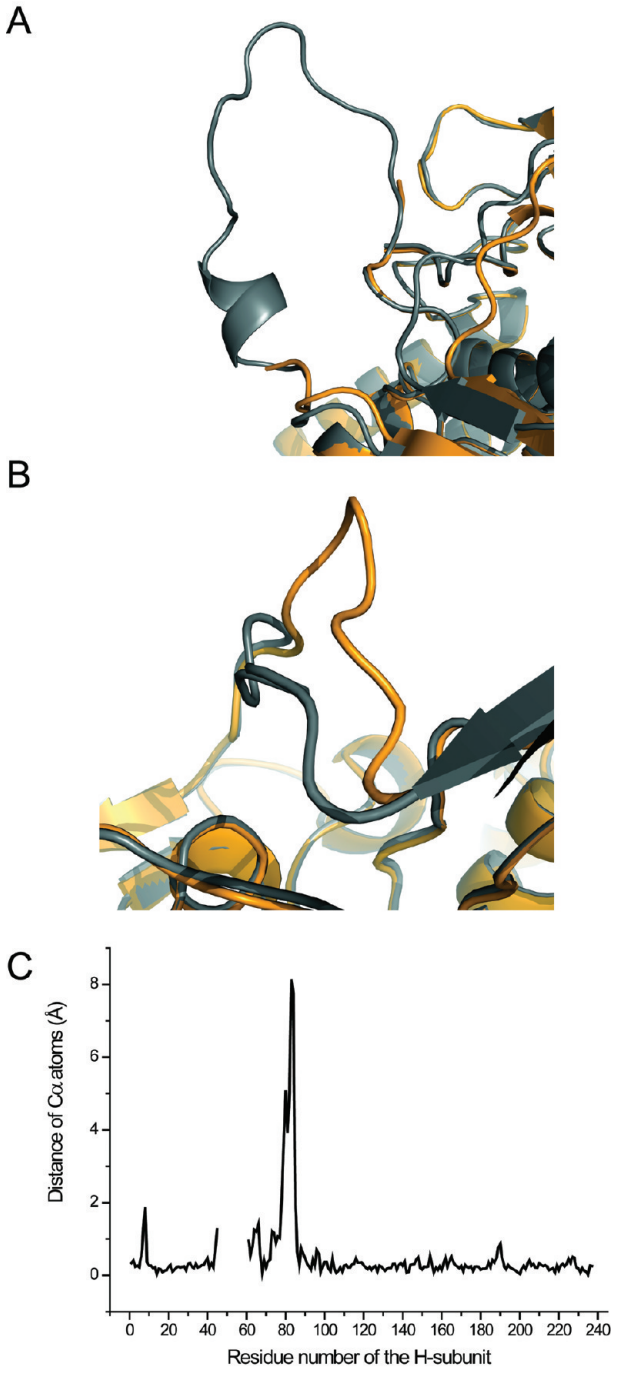

FIGURE 3: Crystal structure comparison of RC_{vir} crystallized using the LSP method (orange, PDB entry 2WJM) and detergent-based method (gray, PDB entry 2PRC). (A) The missing loop in the LSP-grown crystals between residues 46 and 60 of the H-subunit is magnified. This region is involved in crystal contacts between neighboring molecules in detergent-based crystals. (B) The modified loop (Arg-H80 to Thr-H85) of the H-subunit illustrates the area that contributes to the crystal contacts for the LSP structure. (C) Distance plot of the H-subunit between the LSP and the detergent-based model of RC_{vir}.

in a close crystal contact may be affected. In the case of Cys-C1, however, the closest crystal contact is more than 30 Å away.

Extended, Continuous Electron Density Feature Bound to the Hydrophobic Surface of the Reaction Center. In both low- and high-dose data sets a very long (~36 Å) continuous electron density feature was observed to lie within a groove in the membrane region bordered by the transmembrane helix of the H-subunit, the L-subunit, and cofactors of the L-branch. Figure 5

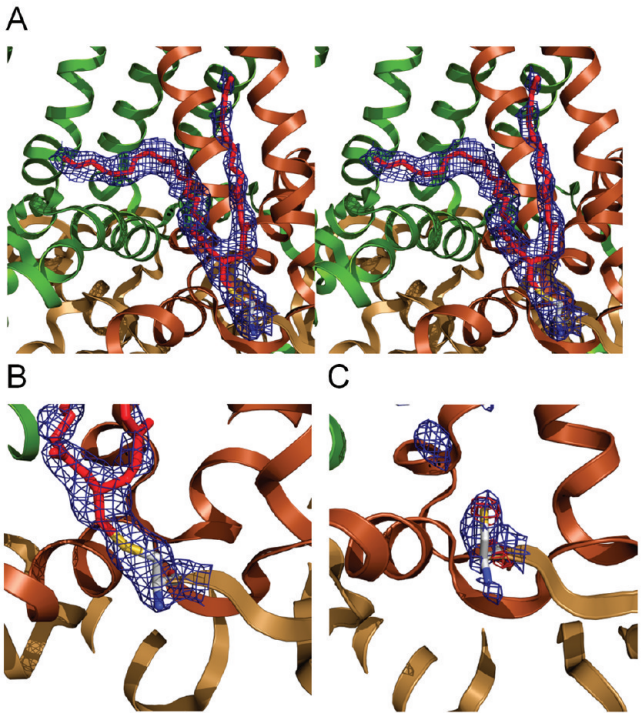

FIGURE 4: (A) The position of the diacylglycerol molecule observed in the $2F_o - F_c$ electron density (0.5σ level, blue) of the low-dose data set is shown in stereoview. (B) Close-up view of the N-terminal cysteine residue of the tetraheme cytochrome *c* subunit to which the diacylglycerol molecule is bound through a thioether bond ($2F_o - F_c$, 1.0σ level, blue). (C) Illustration of the $2F_o - F_c$ electron density at 1.0σ contour level (blue) and the negative $F_o - F_c$ electron density peak on the sulfur of N-terminal cysteine contoured at -4.0σ level (red) in the high-dose data set. The $2F_o - F_c$ electron density is not continuous in the high-dose data set, indicating that the radiation damage breaks the thioether bond.

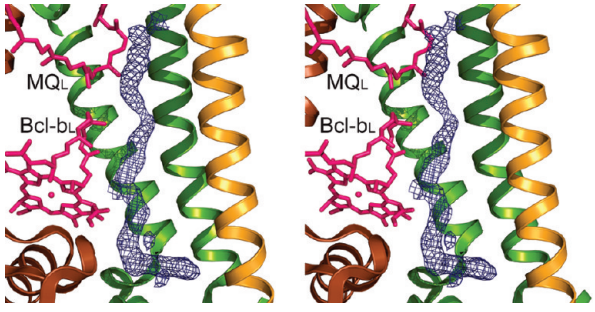

FIGURE 5: Stereoview of the large electron density feature that is located in a groove surrounded by transmembrane helices of the H- (orange) and M-subunit (green) and the cofactors of the L-branch (magenta), stretching the entire membrane of RC_{vir}. The omit $2F_o - F_c$ electron density (blue) from the low-dose data set is contoured at 0.9σ level and stretches perpendicularly to the membrane plane. Supporting Information Figure 2 shows the $2F_o - F_c$ omit electron density recovered from the high-dose data set.

shows the omit $2F_o - F_c$ electron density at 0.9σ contour level observed in the low-dose data set. The higher absorbed dose does not affect the shape of the electron density (Supporting Information Figure 2). The putative lipid corresponding to this electron density feature is approximately perpendicular to the membrane plane and stretches across the whole membrane bilayer. In earlier crystal structures (PDB entry 2PRC) (*19*) electron density in the same binding site was modeled as LDAO molecules, and presumably the electron density was not continuous in the entire binding groove. In the lipidic sponge phase-grown crystal form, the length of

the electron density is more than twice the length of an LDAO molecule and even exceeds the length of membrane-specific fatty acids in their fully extended conformation (~20 Å).

A high proportion of previous crystal structures of reaction centers from *R. sphaeroides* indicated the presence of a cardiolipin molecule (*8*, *30*, *41*−*43*). None of the structures of RC_{vir} in the PDB include cardiolipin, although some contain phosphates or detergents modeled into small electron density features at the equivalent position on the protein surface. The LSP-grown RC_{vir} crystal structure gave similar results to the previous forms, with two electron density features that were modeled as phosphate ions but no indication of a more extensive cardiolipin molecule. In this crystal structure, however, they are not involved in crystal contacts as in the LCP structure of RC_{sph} (*8*).

Monoolein at the Ubiquinone Binding Site. The ubiquinone binding site of RC_{vir} was occupied with a ubiquinone-1 molecule in the original structure obtained from the native source using detergent-based crystallization methods (*36*). Several attempts to model a ubiquinone molecule into the binding pocket of our structure failed, due to the architecture of its headgroup consisting of a quinone ring which includes two methoxy groups, one methyl group, and two additional oxygen atoms. When modeling the ubiquinone headgroup, negative $F_o - F_c$ electron density surrounded it, indicating that it is most likely not pure ubiquinone that occupies the binding pocket. In addition, the isoprenoid tail of Q_B includes branching methyl groups, which did not fit the density very well.

An alternative candidate for the binding pocket is monoolein, the lipid used during crystallization, which is abundantly available. Monoolein is a monoacylglycerol with a small headgroup, and it could be placed in the Q_B binding site with no residual negative $F_o - F_c$ density. Figure 2 shows the full length of this monoolein molecule (cyan). The hydrogen bonds between the hydroxyl groups of the headgroup and the surrounding amino acids were also well satisfied (Figure 6A). The fatty acid tail of monoolein was fully visible on the protein surface, indicating that hydrophobic binding interactions in RC_{vir} are not selective (Figure 2). The initial segment of fatty acid tail, immediately after the ester bond, occupies a position similar to the tail of the semiquinone in the charge-separated conformation in RC_{sph} (PDB entry 1AIG) (*44*). However, the tail of the semiquinone turns around and runs approximately parallel with the membrane, while in the LSP-based crystal form the distal part of monoolein is straighter and turns toward the middle of the membrane. The position of the fatty acid tail is stabilized by weak van der Waals interactions with Val-L182, Leu-L232, Leu-L236, Phe-L235, Phe-L179, the phytyl tail of the accessory bacteriochlorophyll of the M-branch, and one of the fatty acid tails of the bound diacylglycerol.

The ubiquinone binding pocket is strongly conserved in bacterial reaction centers; thus all amino acids interacting with the ubiquinone headgroup (Asn-L213, Glu-L212, His-L190, Leu-L193, Phe-L216, and Ser-L223) of RC_{vir} (Figure 6A,B) and RC_{sph} (Figure 6C,D) are the same. Both Q_B sites are inhibited by herbicides terbutryn, atrazine, and stigmatellin (*9*, *45*−*47*). In addition, the D1 subunit of PSII has a slightly more open, but similar Q_B binding pocket, and it is also inhibited by herbicides. Therefore, it is reasonable to assume that the Q_B binding pockets from different species behave in a similar way when subjected to different lipidic environments.

To test the influence of monoolein, we studied the occupancy of Q_B in a related reaction center from *R. sphaeroides* in

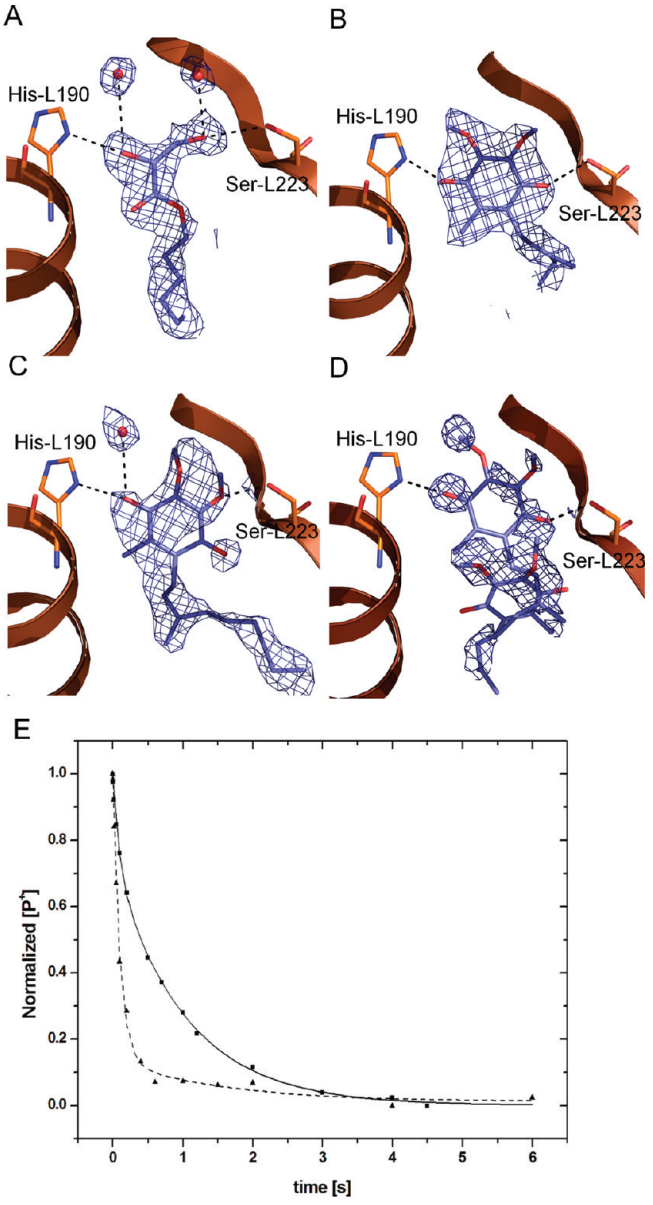

FIGURE 6: (A) Ubiquinone binding pocket of RC_{vir} filled with the lipid monoolein ($2F_o - F_c$ density at 1.2σ level in the low-dose structure). The smaller headgroup of monoolein in comparison to ubiquinone fits the electron density, and the hydrogen bonds with the surrounding amino acids and water molecules are satisfied well. (B) The binding pocket of RC_{vir} in the traditional detergent-based crystal (PDB entry 1VRN (*29*), $2F_o - F_c$ density at 1.2σ level) clearly contains a ubiquinone molecule. (C) The same binding pocket in the LSP-based RC_{sph} (PDB entry 2GNU) (*11*) partially occupied with a ubiquinone molecule. At 1.2σ level the $2F_o - F_c$ electron density shows distinct similarity to (A). (D) In the detergent-based crystal structures of RC_{sph} (e.g., PDB entry 2J8C (*30*), $2F_o - F_c$ density at 1.2 σ level) the electron density shows often significant disorder, and a proximal and distal binding site of ubiquinone can be identified. (E) P^+ recombination kinetics of RC_{sph} measured at 865 nm in detergent solution (squares) and in LSP-grown crystals (triangles). In this example the following rate constants and amplitudes were derived from fitting biexponential decays: RC_{sph} LDAO solution, k_1 = 10.5 s^{-1} (27%) and k_2 = 0.98 s^{-1} (73%), and RC_{sph} LSP crystal, k_1 = 9.7 s^{-1} (87%) and k_2 = 0.68 s^{-1} (13%). The solid and the dotted lines are the modeled biexponential decays.

LSP-grown crystals compared to detergent solution. Spectroscopic techniques are well suited for comparing functional states of crystals and solutions of proteins (*48*−*50*). Therefore, we monitored the charge recombination kinetics of the special pair,

$P^+ \rightarrow P$, by following its absorption change in a microspectrophotometer (*33*). Unlike RC_{vir}, RC_{sph} does not contain a tetraheme cytochrome *c* subunit, and hence the rereduction of the special pair can only occur through charge recombination, and the P^+ decay can be fitted to a sum of two exponentials, corresponding to the recombination of the $P^+Q_A^-$ and the $P^+Q_B^-$ states (*51*). Recombination from the $P^+Q_A^-$ state occurs with a reaction time that is approximately 10-fold shorter than that of the $P^+Q_B^-$ state (*52*). Assuming that charge separation and recombination occur via similar mechanisms in crystals and in solution, the average fractional occupancy of the Q_B site can be estimated from the relative contribution of the amplitude of the slow phase (*51*, *53*). Time-resolved absorption spectroscopic measurements from six different RC_{sph} crystals showed a reduced amplitude of the slow phase in the P^+ decay of RC_{sph} in crystals (dotted line) as compared to that in detergent solution (solid line) (Figure 6E). The average occupancy of Q_B was calculated to be $20 \pm 10\%$, which may not be possible to detect unambiguously by X-ray crystallography, as compared to $50 \pm 10\%$ found for RC_{sph} in detergent solution.

Crystal structures of RC_{sph} grown from the LCP and LSP, respectively, did not always indicate the presence of a ubiquinone headgroup (*8*, *11*), and in the detergent-based crystal structure the occupancy of the bound ubiquinone was estimated to be 30% (*36*). If we contour the electron density at higher contour level, then the most dominant chemical species within the Q_B pocket are highlighted. At 1.2σ contour level the electron density appear to be very similar in the LSP-grown crystal structures of RC_{vir} and RC_{sph} and resembles to a linear headgroup (Figure 6A,C). Beyond the transient kinetics experiment performed on LSP-grown RC_{sph} crystals, the dominant electron density features in the Q_B pocket also appear to be strongly influenced by the crystallization (lipidic) environment.

The influence of phospholipids on ubiquinone binding was also observed in artificial vesicles, with most marked decrease of binding in phosphoglycerol vesicles (*54*). In vesicles containing phosphoglycerol lipids the amplitude of the slow recombination decreased similarly as in the monoolein containing LSP-grown crystals (Table 1 in ref *54*). Phosphoglycerol lipids are characteristic components of photosynthetic membranes (*55*), and the terminal glycerol moiety of phosphoglycerol lipids is also exposed in a similar manner as in monoolein and may have a basal affinity to the Q_B binding pocket. A detergent molecule was also observed in the vicinity of Q_B binding site in a ubiquinone-depleted crystal structure (*19*); however, the lauryl tail of LDAO is bound to a different part of the protein surface. Temperature-dependent spectroscopic measurements highlighted that the Q_B site exhibits marked flexibility, which is essential for the electron transport from Q_A to Q_B, both in bacterial reaction centers (*56*) and in PSII (*57*). Taken together, these observations imply the disorder frequently observed in the Q_B binding pocket may not solely be the consequence of the different conformations and reduction levels of the ubiquinone molecules (*44*) but also due to the inherent flexibility of the Q_B binding pocket and the presence of competing molecules.

CONCLUSION

This work establishes the potential of LSP crystallization for structural studies of the photosynthetic reaction center from *B. viridis*, which possesses relatively large hydrophilic domains. This has previously been considered as a limiting factor for the LCP method due to its limited pore size. The crystal structure reveals intricate details of protein−lipid interactions. In this context, we observed a posttranslational modification by a diacylglycerol molecule covalently bound to the N-terminus of the tetraheme cytochrome *c* subunit of RC_{vir}. We also studied the effect of X-ray radiation damage on the crystal structure and found that the thioether bond of the diacylglycerol is particularly sensitive to higher X-ray doses. A monoolein molecule was found in the Q_B binding pocket, indicating that competing lipid molecules may occupy the mobile ubiquinone binding site.

ACKNOWLEDGMENT

We acknowledge expert experimental support from the staff at beamlines ESRF ID14-eh3 and SLS X06SA.

SUPPORTING INFORMATION AVAILABLE

Schematic representation of the reaction center tilt in the membrane (Figure 1) and $2F_o - F_c$ electron density of the unidentified lipid in the high-dose data set (Figure 2). This material is available free of charge via the Internet at http://pubs.acs.org.

REFERENCES

1. Berg, J. M., Tymoczko, J. L., Stryer, L., and Clarke, N. D. (2002) Biochemistry , 5th ed., W. H. Freeman and Co., New York.
2. Xiong, J., Fischer, W. M., Inoue, K., Nakahara, M., and Bauer, C. E. (2000) Molecular evidence for the early evolution of photosynthesis. *Science 289*, 1724–1730.
3. Raymond, J., Zhaxybayeva, O., Gogarten, J. P., Gerdes, S. Y., and Blankenship, R. E. (2002) Whole-genome analysis of photosynthetic prokaryotes. *Science 298*, 1616–1620.
4. Deisenhofer, J., Epp, O., Miki, K., Huber, R., and Michel, H. (1985) Structure of the protein subunits in the photosynthetic reaction centre of *Rhodopseudomonas viridis* at 3 Å resolution. *Nature 318*, 618–624.
5. Li, L., Mustafi, D., Fu, Q., Tereshko, V., Chen, D. L., Tice, J. D., and Ismagilov, R. F. (2006) Nanoliter microfluidic hybrid method for simultaneous screening and optimization validated with crystallization of membrane proteins. *Proc. Natl. Acad. Sci. U.S.A. 103*, 1 9243–19248.
6. Landau, E. M., and Rosenbusch, J. P. (1996) Lipidic cubic phases: A novel concept for the crystallization of membrane proteins. *Proc. Natl. Acad. Sci. U.S.A. 93*, 14532–14535.
7. Chiu, M. L., Nollert, P., Loewen, M. C., Belrhali, H., Pebay-Peyroula, E., Rosenbusch, J. P., and Landau, E. M. (2000) Crystallization *in cubo*: general applicability to membrane proteins. *Acta Crystallogr. 56*, 781–784.
8. Katona, G., Andreasson, U., Landau, E. M., Andreasson, L. E., and Neutze, R. (2003) Lipidic cubic phase crystal structure of the photosynthetic reaction centre from *Rhodobacter sphaeroides* at 2.35 Å resolution. *J. Mol. Biol. 331*, 681–692.
9. Katona, G., Snijder, A., Gourdon, P., Andreasson, U., Hansson, O., Andreasson, L. E., and Neutze, R. (2005) Conformational regulation of charge recombination reactions in a photosynthetic bacterial reaction center. *Nat. Struct. Mol. Biol. 12*, 630–631.
10. Wöhri, A. B., Johansson, L. C., Wadsten-Hindrichsen, P., Wahlgren, W. Y., Fischer, G., Horsefield, R., Katona, G., Nyblom, M., Oberg, F., Young, G., Cogdell, R. J., Fraser, N. J., Engstrom, S., and Neutze, R. (2008) A lipidic-sponge phase screen for membrane protein crystallization. *Structure 16*, 1003–1009.
11. Wadsten, P., Wöhri, A. B., Snijder, A., Katona, G., Gardiner, A. T., Cogdell, R. J., Neutze, R., and Engström, S. (2006) Lipidic sponge phase crystallization of membrane proteins. *J. Mol. Biol. 364*, 44–53.
12. Johansson, L. C., Wohri, A. B., Katona, G., Engstrom, S., and Neutze, R. (2009) Membrane protein crystallization from lipidic phases. *Curr. Opin. Struct. Biol. 19*, 372–378.
13. Cherezov, V., Yamashita, E., Liu, W., Zhalnina, M., Cramer, W. A., and Caffrey, M. (2006) In *meso* structure of the cobalamin transporter, BtuB, at 1.95 Å resolution. *J. Mol. Biol. 364*, 716–734.
14. Cherezov, V., Clogston, J., Papiz, M. Z., and Caffrey, M. (2006) Room to move: crystallizing membrane proteins in swollen lipidic mesophases. *J. Mol. Biol. 357*, 1605–1618.

15. Gardiner, A. T., Zech, S. G., MacMillan, F., Kass, H., Bittl, R., Schlodder, E., Lendzian, F., and Lubitz, W. (1999) Electron paramagnetic resonance studies of zinc-substituted reaction centers from *Rhodopseudomonas viridis*. *Biochemistry 38*, 11773–11787.
16. Kabsch, W. (1993) Automatic processing of rotation diffraction data from crystals of initially unknown symmetry and cell constants. *J. Appl. Crystallogr. 26*, 795–800.
17. Collaborative computational project number 4 (1994) The CCP4 suite: programs for protein crystallography. *Acta Crystallogr. 50*, 760–763.
18. Navaza, J. (1994) AMoRe: an automated package for molecular replacement. *Acta Crystallogr. 50*, 157–163.
19. Lancaster, C. R., and Michel, H. (1997) The coupling of light-induced electron transfer and proton uptake as derived from crystal structures of reaction centres from *Rhodopseudomonas viridis* modified at the binding site of the secondary quinone, QB. *Structure 5*, 1339–1359.
20. Lamzin, V. S., and Wilson, K. S. (1993) Automated refinement of protein models. *Acta Crystallogr. 49*, 129–147.
21. Emsley, P., and Cowtan, K. (2004) Coot: model-building tools for molecular graphics. *Acta Crystallogr. 60*, 2126–2132.
22. Murshudov, G. N., Vagin, A. A., and Dodson, E. J. (1997) Refinement of macromolecular structures by the maximum-likelihood method. *Acta Crystallogr. 53*, 240–255.
23. Read, R. J. (1986) Improved Fourier coefficients for maps using phases from partial structures with errors. *Acta Crystallogr. 42*, 140–149.
24. Schomaker, V., and Trueblood, K. N. (1968) On the rigid-body motion of molecules in crystals. *Acta Crystallogr. B24*, 63–76.
25. Laskowski, R. A., MacArthur, M. W., Moss, D. S., and Thornton, J. M. (1993) PROCHECK: a program to check the stereochemical quality of protein structures. *J. Appl. Crystallogr. 26*, 283–291.
26. Davis, I. W., Leaver-Fay, A., Chen, V. B., Block, J. N., Kapral, G. J., Wang, X., Murray, L. W., Arendall, W. B.III, Snoeyink, J., Richardson, J. S., and Richardson, D. C. (2007) MolProbity: all-atom contacts and structure validation for proteins and nucleic acids. *Nucleic Acids Res. 35*, W375–W383.
27. Paithankar, K. S., Owen, R. L., and Garman, E. F. (2009) Absorbed dose calculations for macromolecular crystals: improvements to RADDOSE. *J. Synchrotron Radiat. 16*, 152–162.
28. Kleywegt, G. J. (1999) Experimental assessment of differences between related protein crystal structures. *Acta Crystallogr. 55*, 1878–1884.
29. Baxter, R. H., Seagle, B. L., Ponomarenko, N., and Norris, J. R. (2005) Cryogenic structure of the photosynthetic reaction center of *Blastochloris viridis* in the light and dark. *Acta Crystallogr. 61*, 605–612.
30. Koepke, J., Krammer, E. M., Klingen, A. R., Sebban, P., Ullmann, G. M., and Fritzsch, G. (2007) pH modulates the quinone position in the photosynthetic reaction center from *Rhodobacter sphaeroides* in the neutral and charge separated states. *J. Mol. Biol. 371*, 396–409.
31. Kleywegt, G. J., Harris, M. R., Zou, J. Y., Taylor, T. C., Wahlby, A., and Jones, T. A. (2004) The Uppsala Electron Density Server. *Acta Crystallogr. 60*, 2240–2249.
32. DeLano, W. L. (2002) The PyMOL Molecular Graphics System, DeLano Scientific, San Carlos, CA.
33. Hadfield, A., and Hajdu, J. (1993) A fast and portable microspectrophotometer for protein crystallography. *J. Appl. Crystallogr. 26*, 839–842.
34. Gourdon, P., Alfredsson, A., Pedersen, A., Malmerberg, E., Nyblom, M., Widell, M., Berntsson, R., Pinhassi, J., Braiman, M., Hansson, O., Bonander, N., Karlsson, G., and Neutze, R. (2008) Optimized in vitro and in vivo expression of proteorhodopsin: a seven-transmembrane proton pump. *Protein Expression Purif. 58*, 103–113.
35. Berman, H. M., Westbrook, J., Feng, Z., Gilliland, G., Bhat, T. N., Weissig, H., Shindyalov, I. N., and Bourne, P. E. (2000) The Protein Data Bank. *Nucleic Acids Res. 28*, 235–242.
36. Deisenhofer, J., Epp, O., Sinning, I., and Michel, H. (1995) Crystallographic refinement at 2.3 Å resolution and refined model of the photosynthetic reaction centre from *Rhodopseudomonas viridis*. *J. Mol. Biol. 246*, 429–457.
37. Deisenhofer, J., and Michel, H. (1989) Nobel lecture. The photosynthetic reaction centre from the purple bacterium *Rhodopseudomonas viridis*. *EMBO J. 8*, 2149–2170.
38. Escriba, P. V., Wedegaertner, P. B., Goni, F. M., and Vogler, O. (2007) Lipid-protein interactions in GPCR-associated signaling. *Biochim. Biophys. Acta 1768*, 836–852.
39. Ravelli, R. B., and Garman, E. F. (2006) Radiation damage in macromolecular cryocrystallography. *Curr. Opin. Struct. Biol. 16*, 624–629.
40. Henderson, R. (1990) Cryo-protection of protein crystals against radiation damage in electron and X-ray diffraction. *Proc. R. Soc. London, Ser. B 241*, 6–8.
41. Camara-Artigas, A., Brune, D., and Allen, J. P. (2002) Interactions between lipids and bacterial reaction centers determined by protein crystallography. *Proc. Natl. Acad. Sci. U.S.A. 99*, 11055–11060.
42. McAuley, K. E., Fyfe, P. K., Ridge, J. P., Isaacs, N. W., Cogdell, R. J., and Jones, M. R. (1999) Structural details of an interaction between cardiolipin and an integral membrane protein. *Proc. Natl. Acad. Sci. U.S.A. 96*, 14706–14711.
43. Fyfe, P. K., Isaacs, N. W., Cogdell, R. J., and Jones, M. R. (2004) Disruption of a specific molecular interaction with a bound lipid affects the thermal stability of the purple bacterial reaction centre. *Biochim. Biophys. Acta 1608*, 11–22.
44. Stowell, M. H., McPhillips, T. M., Rees, D. C., Soltis, S. M., Abresch, E., and Feher, G. (1997) Light-induced structural changes in photosynthetic reaction center: implications for mechanism of electron-proton transfer. *Science 276*, 812–816.
45. Lancaster, C. R., Bibikova, M. V., Sabatino, P., Oesterhelt, D., and Michel, H. (2000) Structural basis of the drastically increased initial electron transfer rate in the reaction center from a *Rhodopseudomonas viridis* mutant described at 2.00 Å resolution. *J. Biol. Chem. 275*, 39364–39368.
46. Lancaster, C. R., Hunte, C., Kelley, J.III, Trumpower, B. L., and Ditchfield, R. (2007) A comparison of stigmatellin conformations, free and bound to the photosynthetic reaction center and the cytochrome *bc1* complex. *J. Mol. Biol. 368*, 197–208.
47. Lancaster, C. R., and Michel, H. (1999) Refined crystal structures of reaction centres from *Rhodopseudomonas viridis* in complexes with the herbicide atrazine and two chiral atrazine derivatives also lead to a new model of the bound carotenoid. *J. Mol. Biol. 286*, 883–898.
48. De la Mora-Rey, T., and Wilmot, C. M. (2007) Synergy within structural biology of single crystal optical spectroscopy and X-ray crystallography. *Curr. Opin. Struct. Biol. 17*, 580–586.
49. Katona, G., Carpentier, P., Niviere, V., Amara, P., Adam, V., Ohana, J., Tsanov, N., and Bourgeois, D. (2007) Raman-assisted crystallography reveals end-on peroxide intermediates in a nonheme iron enzyme. *Science 316*, 449–453.
50. Bourgeois, D., and Royant, A. (2005) Advances in kinetic protein crystallography. *Curr. Opin. Struct. Biol. 15*, 538–547.
51. Tiede, D. M., Vazquez, J., Cordova, J., and Marone, P. A. (1996) Time-resolved electrochromism associated with the formation of quinone anions in the *Rhodobacter sphaeroides* R26 reaction center. *Biochemistry 35*, 10763–10775.
52. Clayton, R. K., and Yau, H. F. (1972) Photochemical electron transport in photosynthetic reaction centers from *Rhodopseudomonas spheroides*. I. Kinetics of the oxidation and reduction of P-870 as affected by external factors. *Biophys. J. 12*, 867–881.
53. Kleinfeld, D., Okamura, M. Y., and Feher, G. (1984) Electron transfer in reaction centers of *Rhodopseudomonas sphaeroides*. I. Determination of the charge recombination pathway of D+QAQ-(−)B and free energy and kinetic relations between Q(−)AQ_B and QAQ(−)B. *Biochim. Biophys. Acta 766*, 126–140.
54. Nagy, L., Milano, F., Dorogi, M., Agostiano, A., Laczko, G., Szebenyi, K., Varo, G., Trotta, M., and Maroti, P. (2004) Protein/lipid interaction in the bacterial photosynthetic reaction center: phosphatidylcholine and phosphatidylglycerol modify the free energy levels of the quinones. *Biochemistry 43*, 12913–12923.
55. Wood, B. J., Nichols, B. W., and James, A. T. (1965) The lipids and fatty acid metabolism of photosynthetic bacteria. *Biochim. Biophys. Acta 106*, 261–273.
56. Parak, F., Frolov, E. N., Kononenko, A. A., Mossbauer, R. L., Goldanskii, V. I., and Rubin, A. B. (1980) Evidence for a correlation between the photoinduced electron transfer and dynamic properties of the chromatophore membranes from *Rhodospirillum rubrum*. *FEBS Lett. 117*, 368–372.
57. Garbers, A., Reifarth, F., Kurreck, J., Renger, G., and Parak, F. (1998) Correlation between protein flexibility and electron transfer from Q_A^-* to Q_B in PSII membrane fragments from spinach. *Biochemistry 37*, 11399–11404.